

# Left-right splitting of elliptic flow due to directed flow in heavy ion collisions

Chao Zhang<sup>1,2</sup> and Zi-Wei Lin<sup>3,\*</sup>

<sup>1</sup>*Department of Physics, East Carolina University, Greenville, NC 27858, USA*

<sup>2</sup>*Institute of Particle Physics and Key Laboratory of Quark & Lepton Physics (MOE),  
Central China Normal University, Wuhan 430079, China*

<sup>3</sup>*Department of Physics, East Carolina University, Greenville, North Carolina 27858, USA*

Recently the splitting of elliptic flow  $v_2$  at finite rapidities has been proposed as a result of the global vorticity in non-central relativistic heavy ion collisions. In this study, we find that this left-right (i.e., on opposite sides of the impact parameter axis) splitting of the elliptic flow at finite rapidities is a result of the non-zero directed flow  $v_1$ , with the splitting magnitude  $\approx 8v_1(1 - 3v_2)/(3\pi)$ . We also use a multi-phase transport model, which automatically includes the vorticity field and flow fluctuations, to confirm the  $v_2$  splitting. In addition, we find that the analytical expectations for the  $v_2$  splitting work for the raw  $v_2$  and  $v_1$  (i.e., before event plane resolutions are applied) measured relative to either the first- or second-order event plane. Since the  $v_2$  splitting is mostly driven by  $v_1$ , it vanishes at zero transverse momentum ( $p_T$ ), and its magnitude and sign may have non-trivial dependencies on  $p_T$ , centrality, collision energy, and hadron species.

## I. INTRODUCTION

Heavy ion collisions provide us a way to study the properties of the created matter in relation to the theory of quantum chromodynamics. At high-enough energies, the created matter should be initially deconfined and be represented by parton degrees of matter, the quark-gluon plasma (QGP) [1]. Anisotropic flows in the final particle momentum distribution are powerful tools to study heavy ion physics [2]. They include the directed flow  $v_1$ , elliptic flow  $v_2$ , the more recently discovered triangular flow  $v_3$  [3], and higher-order flows. Significant anisotropic flows have been observed in non-central heavy ion collisions [4–6], while they have also been observed in small systems such as  $p$ +Au,  $d$ +Au, He+Au [7], and  $p$ +Pb [8] collisions at high energies. It is well known that the initial geometry of the overlap volume in a heavy ion collision has a fluctuating and complicated event-by-event three-dimensional structure, and the initial spatial anisotropies are converted into anisotropic flows in momentum through particle interactions in transport models or the pressure gradient in hydrodynamical models. On the other hand, the origin of flow-like behavior in small systems including  $p + p$  collisions is still under debate, where initial-state correlations [9, 10], the parton escape mechanism [11, 12] or kinetic theory [13, 14], and hydrodynamics [15, 16] have been proposed as the dominant mechanism.

Recently, the splitting of elliptic flow on opposite sides of the impact parameter axis has been proposed as a new observable [17], where it is argued to be the result of the global vorticity in non-central relativistic heavy ion collisions. In this study, we examine this  $v_2$  splitting in A+A collisions at RHIC and LHC energies.

## II. METHOD

After a brief analysis of the left-right  $v_2$  splitting that relates it to  $v_1$ , we shall use a multi-phase transport (AMPT) model [18, 19] to test the relationship. The AMPT model is an event generator for relativistic heavy ion collisions that contains four parts: the fluctuating initial condition based on the HIJING model, the parton cascade model ZPC for elastic scatterings, a spatial quark coalescence model to describe the hadronization, and a hadron cascade. The string melting version of the AMPT model [18, 20] is applicable at high energies when the QGP is expected to be formed. It has been shown to well describe the bulk matter including the overall elliptic flow [20, 21] and the vorticity field [22, 23] in heavy ion collisions. Its fluctuating initial condition also creates spatial anisotropies that lead to anisotropic flows of different orders [3]. Recently we have updated the AMPT model with a new quark coalescence model [24], modern parton distribution functions in nuclei [25], and improved heavy quark productions [26]. In addition, we have applied local nuclear scaling to two key parameters in the AMPT initial condition, which enables the model to self-consistently describe the system size and centrality dependence of nuclear collisions [19]. For this study, we employ the string melting version of the AMPT model that contains the above improvements.

In the AMPT model [18], the  $x$ -axis is along the impact parameter ( $\vec{b}$ ) in the transverse plane of each event, where the centers of the projectile and target nuclei are at the transverse position  $(b/2, 0)$  and  $(-b/2, 0)$ , respectively. The direction of the projectile momentum specifies the  $z$ -axis; as a result, the total angular momentum of the system is along the  $-y$  direction [22]. Note that this coordinate system is the same as that in the recent study that first proposed the  $v_2$  splitting [17]. In Sec.III, we analyze the  $v_2$  splitting and calculate flows using the theoretical reaction plane for simplicity. Then in Sec.IV we use the experimental event plane method to calculate

\* linz@ecu.edu

the flows and  $v_2$  splitting.

### III. RESULTS USING THE REACTION PLANE

Let us write the normalized azimuthal distribution in momentum for particles in a given phase space, e.g., at a given  $p_T$  and rapidity  $y$  or pseudorapidity  $\eta$ , as

$$f(\phi) = \frac{1}{2\pi} \left( 1 + \sum_{n=1}^{\infty} [c_n \cos(n\phi) + s_n \sin(n\phi)] \right). \quad (1)$$

The above gives the usual relations  $\langle \cos \phi \rangle = c_1/2 \equiv v_1$  and  $\langle \cos(2\phi) \rangle = c_2/2 \equiv v_2$  when we integrate over the full range of  $\phi$  in the averaging over particles and events. On the other hand, if we integrate over  $\phi \in (-\pi/2, \pi/2)$  for the  $p_x > 0$  part or over  $\phi \in (\pi/2, 3\pi/2)$  for the  $p_x < 0$  part, we obtain the following for  $v_2$  (with terms up to  $n = 4$ ):

$$v_2(p_x > 0) \equiv \frac{\int_{-\pi/2}^{\pi/2} \cos(2\phi) f(\phi) d\phi}{\int_{-\pi/2}^{\pi/2} f(\phi) d\phi} = \frac{v_2 + \frac{4v_1}{3\pi} + \frac{6c_3}{5\pi}}{1 + \frac{4v_1}{\pi} - \frac{2c_3}{3\pi}},$$

$$v_2(p_x < 0) \equiv \frac{\int_{\pi/2}^{3\pi/2} \cos(2\phi) f(\phi) d\phi}{\int_{\pi/2}^{3\pi/2} f(\phi) d\phi} = \frac{v_2 - \frac{4v_1}{3\pi} - \frac{6c_3}{5\pi}}{1 - \frac{4v_1}{\pi} + \frac{2c_3}{3\pi}}. \quad (2)$$

Note that the coefficient  $c_3 = 2\langle \cos(3\phi) \rangle$  does not correspond to (twice) the usual triangular flow  $v_3$  [3], which axes fluctuate mostly independently of the  $x$ -axis (or the reaction plane). Instead,  $c_3$  here is calculated relative to the reaction plane and represents another type of triangular flow at finite rapidities that correlates with the reaction plane, and it is expected to be rapidity-odd. If  $|c_3| \ll |v_1|$ , we can neglect  $c_3$  and get simpler relations (up to second order in  $v_1$  and/or  $v_2$ ):

$$v_2(p_x > 0) \simeq \frac{v_2 + \frac{4v_1}{3\pi}}{1 + \frac{4v_1}{\pi}} \simeq v_2 - \frac{16v_1^2}{3\pi^2} + \frac{4v_1}{3\pi} (1 - 3v_2),$$

$$v_2(p_x < 0) \simeq \frac{v_2 - \frac{4v_1}{3\pi}}{1 - \frac{4v_1}{\pi}} \simeq v_2 - \frac{16v_1^2}{3\pi^2} - \frac{4v_1}{3\pi} (1 - 3v_2). \quad (3)$$

Therefore, the left-right  $v_2$  splitting at finite rapidities, given by  $v_2(p_x > 0) - v_2(p_x < 0) \simeq 8v_1(1 - 3v_2)/(3\pi)$ , comes directly from the finite directed flow  $v_1$ .

We now use the AMPT model to test these relationships. Figure 1 shows the results of  $v_2(p_T)$  of charged hadrons and final state partons with  $p_x > 0$ ,  $p_x < 0$ , and all  $p_x$  for minimum bias Au+Au collisions at 200A GeV. Results for the pseudorapidity ranges of  $0 < \eta < 2$  and  $-2 < \eta < 0$  are shown in the left and right panels, respectively. We see that the left-right splitting of elliptic flow exists for both partons and hadrons in the final state. The  $v_2$  splitting is small at low  $p_T$  and then become obvious for partons at  $p_T > 1$  GeV/c and for hadrons at  $p_T > 1.5$  GeV/c. In addition, we see that the  $v_2$  splitting is antisymmetric versus  $\eta$ , which is mostly due to

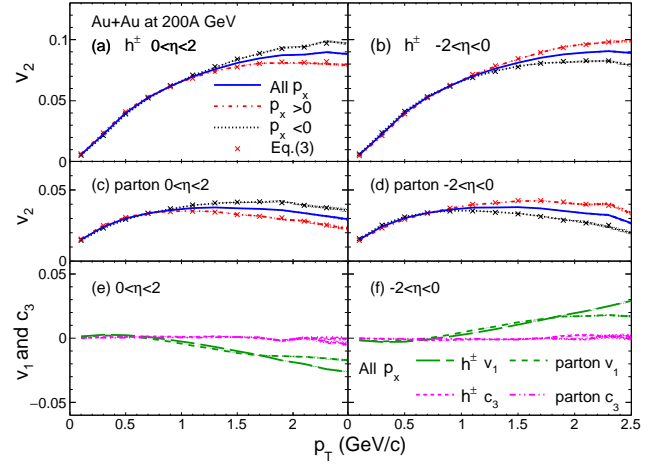


FIG. 1. Left panels show (a)  $v_2$  of charged hadrons, (c)  $v_2$  of partons, (e)  $v_1$  and  $c_3$  within  $0 < \eta < 2$  versus the transverse momentum for minimum bias Au+Au collisions at 200A GeV from the AMPT model. The overall  $v_2$  (solid),  $v_2(p_x > 0)$  (dashed), and  $v_2(p_x < 0)$  (dotted) are shown, while crosses represent the expectations of Eq.(3). The corresponding results for particles within  $-2 < \eta < 0$  are shown in the right panels.

the rapidity-odd  $v_1$  as  $c_3 \simeq 0$  in this figure. Note that we call this the left-right splitting of the elliptic flow  $v_2$ , because particles with  $p_x > 0$  and  $p_x < 0$  are on the right and left side of the impact parameter axis, respectively. This also helps to differentiate it from the  $v_2$  splitting between particles and antiparticles, which has been shown to be sensitive to partonic and hadronic potentials at low energies or high net-baryon chemical potential [27, 28].

We also show in Figs. 1(e) and (f) the overall  $v_1(p_T)$  of charged hadrons and partons at positive and negative pseudorapidities, respectively. The expectations from Eq.(3) using the overall (i.e., all  $p_x$ )  $v_1(p_T)$  and  $v_2(p_T)$  are shown by the cross symbols in Figs. 1(a-d), which agree well with the directly calculated  $v_2$  splitting curves. The good agreements with Eq.(3) in Fig. 1 also indicate  $c_3(p_T) \simeq 0$  there, which we confirm in Figs. 1(e) and (f) with direct calculations of  $c_3(p_T)$  (magenta curves).

Next we investigate the possible centrality dependence of the  $v_2$  splitting in Fig. 2, which shows the AMPT results of  $v_2(p_T)$  for charged hadrons within  $0 < \eta < 2$  for different centralities of Au+Au collisions at 200A GeV. Here centrality is determined with the charged hadron multiplicity within mid-pseudorapidity. We observe the  $v_2$  splitting at all centralities (except for very peripheral collisions where the statistical errors are relatively large). In addition, the order of the splitting at higher  $p_T$ , i.e., the sign of  $v_2(p_x > 0) - v_2(p_x < 0)$ , does not change with centrality here. It is also interesting to see that the  $v_2$  splitting exists even in the most central (0-5%) events.

Figure 3 shows the centrality dependence of the integrated  $v_2$  of charged hadrons with positive or negative  $p_x$  in Au+Au collisions at 200A GeV from the AMPT model. The  $v_2$  integrated over  $p_T > 1.5$  GeV/c shows a

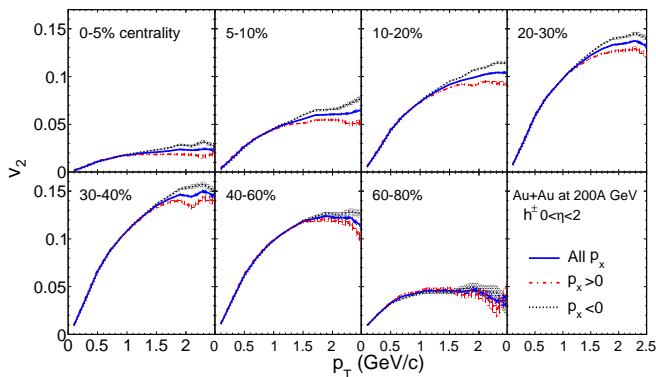


FIG. 2. The overall and split  $v_2(p_T)$  of charged hadrons within  $0 < \eta < 2$  for different centralities of Au+Au collisions at 200A GeV from the AMPT model.

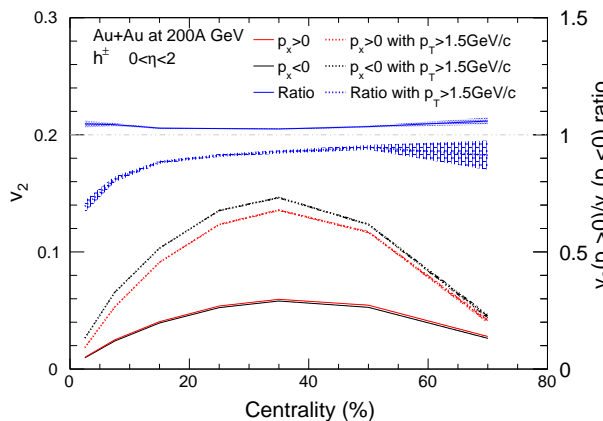


FIG. 3. Centrality dependence of  $p_T$ -integrated  $v_2$  for charged hadrons with positive or negative  $p_x$  and their ratio (blue curves). Solid and dotted  $v_2$  curves represent the results integrated over all  $p_T$  and over  $p_T > 1.5$  GeV/c, respectively.

significant left-right splitting, consistent with that shown in Fig. 2. On the other hand, the  $v_2$  integrated over all  $p_T$  shows a very small splitting, while the order of splitting is also opposite to that of the  $v_2$  integrated over  $p_T > 1.5$  GeV/c. This is because the directed flow  $v_1$  from the AMPT model changes sign at  $p_T \sim 0.7$  GeV/c, as shown in Fig. 1. We also show in Fig. 3 the ratio  $v_2(p_x > 0)/v_2(p_x < 0)$  to represent the relative left-right  $v_2$  splitting. While the ratio of the split  $v_2$  integrated over all  $p_T$  is rather flat versus centrality, the ratio of the split  $v_2$  integrated over  $p_T > 1.5$  GeV/c shows a significant dependence on centrality, where the relative splitting is the biggest for the most central events. This is possible because, although both  $v_2$  and  $v_1$  usually approach zero for central collisions, the relative  $v_2$  splitting mostly depends on  $v_1/v_2$ , which could be large.

In Fig. 4 we examine the  $v_2$  splitting at different energies at RHIC and LHC, where the upper panels (a-c) show the AMPT  $v_2(p_T)$  results of charged hadrons within

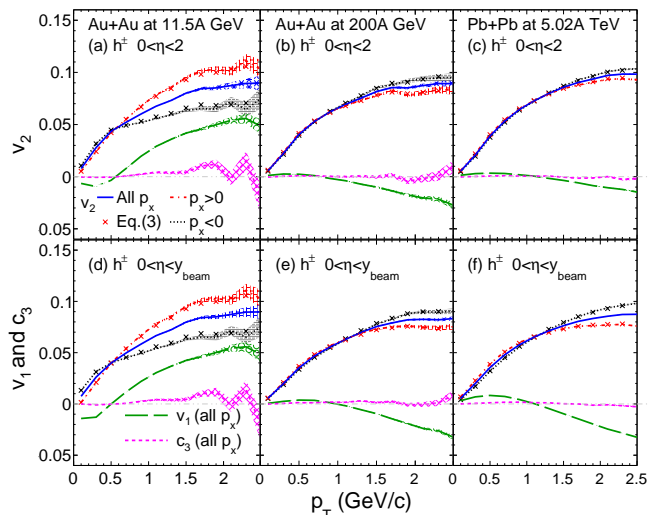


FIG. 4. The overall  $v_2$  (solid),  $v_2(p_x > 0)$  (dot-dashed),  $v_2(p_x < 0)$  (dotted),  $v_1$  (long-dashed), and  $c_3$  (dashed) of charged hadrons within  $0 < \eta < 2$  in minimum bias (a) Au+Au collisions at 11.5A GeV and (c) Pb+Pb collisions at 5.02A TeV. The corresponding results within  $0 < \eta < y_{\text{beam}}$  are shown in the lower panels, while crosses represent the expectations of Eq.(3).

$0 < \eta < 2$  in minimum bias Au+Au collisions at 11.5A and 200A GeV and minimum bias Pb+Pb collisions at 5.02A TeV. The magnitude of the  $v_2$  splitting decreases as the colliding energy increases; this is expected because the directed flow  $v_1$  is usually smaller at higher energies. We also see that the order of splitting can be different at different energies as a result of the sign of  $v_1(p_T)$ . The expectations from Eq.(3), shown as the cross symbols, agree rather well with the split  $v_2$  results at all three energies, although there is a small discrepancy at 11.5A GeV. This discrepancy is due to the  $c_3$  terms in Eq.(2), because  $c_3$  is not very small at 11.5A GeV as shown in Fig. 4(a). In cases where  $|c_3| \ll |v_1|$  is not true, Eq.(3) is not accurate enough while Eq.(2) still is. In the lower panels of Fig 4, we show the split  $v_2(p_T)$  results for charged hadrons within  $0 < \eta < y_{\text{beam}}$ , where  $y_{\text{beam}}$  is the projectile rapidity in the center-of-mass frame of the heavy ion collision. We see that the magnitudes of the  $v_2$  splitting are similar at these different energies, and the wider  $\eta$  range increases the magnitude of  $v_2$  splitting at high energies due to the big  $v_1$  magnitudes at large rapidities. This suggests that the left-right  $v_2$  splitting could be observed even at LHC energies if one looks at large rapidities.

#### IV. RESULTS USING THE EVENT PLANE

So far we have used the theoretical reaction plane (RP) for the flow analysis. We now use the experimental event-plane method to see whether the  $v_2$  splitting can be observed experimentally. Specifically, we use minimum bias

Au+Au collisions at 11.5A GeV as the example. The event plane angle  $\Psi_n$  is calculated with the event-by-event flow vector  $\vec{Q}_n$  [29, 30] according to

$$\begin{aligned} X_n &= \sum_i w_i \cos(n\phi_i), \quad Y_n = \sum_i w_i \sin(n\phi_i), \\ \Psi_n &= \arctan2(Y_n, X_n)/n. \end{aligned} \quad (4)$$

In the above,  $\phi_i$  is the azimuthal angle of the  $i^{\text{th}}$  particle's momentum in the event, and the weight  $w_i$  is taken as the particle transverse momentum. The first-order event plane angle  $\Psi_1$  is reconstructed from two flow vectors:  $\vec{Q}_{1,\text{west}}$  from  $3.5 < \eta < 5.09$  and  $\vec{Q}_{1,\text{east}}$  from  $-5.09 < \eta < -3.5$ . The first-order flow vector of the full event is then reconstructed as  $\vec{Q}_1 = \vec{Q}_{1,\text{west}} - \vec{Q}_{1,\text{east}}$ . Note that we have chosen a narrower  $\eta$  range than the STAR event plane detector (EPD) system [31] to get a better resolution of  $\Psi_1$ . The second-order event plane angle  $\Psi_2$  is reconstructed from the flow vector of particles within  $-2 < \eta < 2$ .

### A. Relative to the first-order event plane $\Psi_1$

Flow coefficients relative to the first-order event plane are calculated as

$$v_n\{\Psi_1\} \equiv \frac{v_n^{\text{obs}}}{R_n\{\Psi_1\}} = \frac{\langle\langle \cos[n(\phi - \Psi_1)] \rangle\rangle}{\langle \cos[n(\Psi_1 - \Psi_r)] \rangle}. \quad (5)$$

In the above,  $\Psi_r$  represents the ‘‘true’’ reaction plane angle, and the numerator represents the observed (or raw) anisotropic flows which are directly measured in the experiments, where the double brackets represent the averaging over particles in each event and then over all events. The denominator represents the event plane resolution, where the single bracket represents the averaging over all events. We follow the two-subevent method [29] to calculate the resolutions, where the two subevents are from  $3.5 < \eta < 5.09$  and  $-5.09 < \eta < -3.5$ , respectively, for calculating  $R_n\{\Psi_1\}$ . Note that we use a modified equation  $R_{2k+1}^{\text{sub}}\{\Psi_1\} = \sqrt{\langle \cos[(2k+1)(\Psi_1^a - \Psi_1^b - \pi)] \rangle}$  instead of  $\sqrt{\langle \cos[(2k+1)(\Psi_1^a - \Psi_1^b)] \rangle}$  [29] to calculate the subevent resolution for the odd-order anisotropies, because  $\Psi_{1,\text{west}}$  for one subevent is expected to be different from  $\Psi_{1,\text{east}}$  for the other subevent by  $\pi$  on average. We then determine the  $\chi_n^{\text{sub}}$  value from  $R_n^{\text{sub}}$ . Using  $\chi_n = \sqrt{2}\chi_n^{\text{sub}}$  for the full event [29], we then obtain the full event resolutions  $R_n\{\Psi_1\}$ .

We show in Fig. 5 the  $v_2$  splitting results relative to the first-order event plane after applying the resolution corrections with  $R_n\{\Psi_1\}$ . Note that here we treat the  $\Psi_1$  angle as the  $x$ -axis, where any hadron with  $\cos(\phi - \Psi_1) > 0$  belongs to the  $p_x > 0$  group. The upper two panels show the overall, left-side and right-side  $v_2$  of charged particles within  $0 < \eta < 2$  and  $-2 < \eta < 0$ , respectively, while the corresponding  $v_1$  and  $c_3$  results are shown in the lower

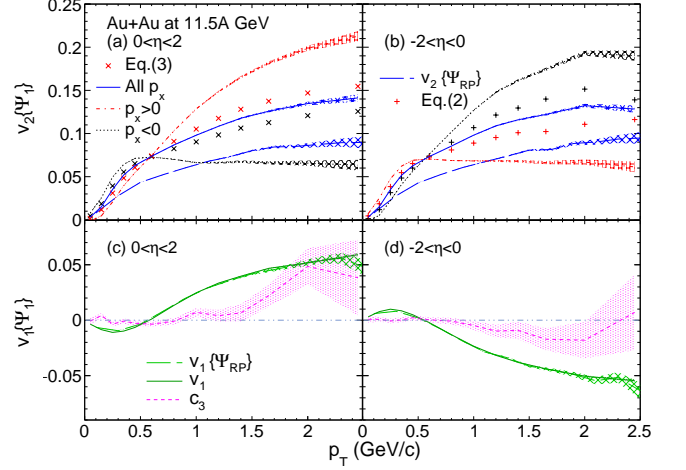


FIG. 5. (a) The overall and split  $v_2$ , and (c)  $v_1$  and  $c_3$  of charged hadrons relative to the first-order event plane angle  $\Psi_1$  versus the transverse momentum for  $0 < \eta < 2$  in minimum bias Au+Au collisions at 11.5A GeV from the AMPT model. Results for  $-2 < \eta < 0$  are shown in the right panels. Cross and plus symbols represent expectations of Eq.(3) and Eq.(2), respectively, and long dashed curves represent  $v_2$  (blue) and  $v_1$  (green) relative to the theoretical reaction plane angle.

panels. The cross symbols in Fig. 5(a) are the expectations of the split  $v_2$  by applying Eq.(3) to the overall  $v_2$  in panel (a) and overall  $v_1$  in panel (c). It is clear that the expectations of Eq.(3) fail here. Since  $c_3$  is not too small here, we also apply Eq.(2) to the overall  $v_2$  in panel (b), and overall  $v_1$  and overall  $c_3$  in panel (d) to obtain the plus symbols; they still fail to describe the split  $v_2$  curves in panel (b). In addition, the long dashed curves in Fig. 5 are the  $v_1\{\Psi_{\text{RP}}\}$  and  $v_2\{\Psi_{\text{RP}}\}$  relative to the theoretical reaction plane, where  $v_1\{\Psi_1\}$  well reproduces  $v_1\{\Psi_{\text{RP}}\}$  while  $v_2\{\Psi_1\}$  are different from  $v_2\{\Psi_{\text{RP}}\}$ .

The raw  $v_2$  splitting results relative to the first-order event plane, i.e., without the resolution corrections, are shown in Fig. 6. We see in panel (a) that the split  $v_2$  results (dot-dashed curve and dotted curve) agree well with the cross symbols, which are obtained by applying Eq.(3) to the overall  $v_1^{\text{obs}}$  and  $v_2^{\text{obs}}$  in the left panels. The split  $v_2$  results in panel (b) also agree well with the plus symbols that are obtained by applying Eq.(2); this is expected since  $c_3 \simeq 0$  in Fig. 6 and thus Eq.(2) and Eq.(3) are essentially the same. Therefore, the raw overall  $v_1$  extracted with Eq. (3) from the split  $v_2$  measurements relative to  $\Psi_1$  can be corrected with its event plane resolution to yield the corrected  $v_1$ , which will be equivalent to the standard  $v_1\{\Psi_1\}$ . It is also apparent that Eq.(2) and Eq.(3) fail in Fig. 5 because of the different resolution values for  $v_1$  and  $v_2$ . Specifically,  $R_1\{\Psi_1\} = 0.574$ ,  $R_2\{\Psi_1\} = 0.188$ , and  $R_3\{\Psi_1\} = 0.047$  are the resolutions used to obtain the corrected  $v_1$ ,  $v_2$ , and  $c_3$  in Fig. 5. In addition, it is interesting to see the large relative  $v_2$  splitting in Fig. 6; this is mostly due to the higher resolution  $R_1\{\Psi_1\}$  than  $R_2\{\Psi_1\}$ , which makes

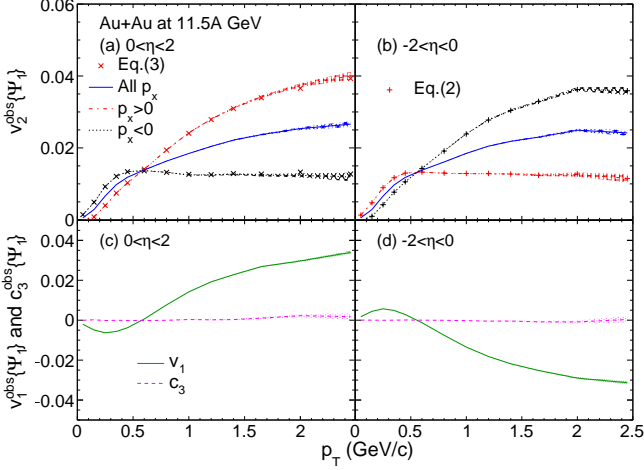


FIG. 6. Same as Fig. 5 but without the resolution corrections; here the  $v_2$  splitting results agree with Eqs.(2)-(3).

$v_1^{\text{obs}}/v_2^{\text{obs}}$  much bigger than the corrected  $v_1/v_2$ .

### B. Relative to the second-order event plane

Here we explore the  $v_2$  splitting analysis relative to the second-order event plane. First, we need to know the second-order event plane angle that points toward the direction of the impact parameter, which we call  $\Psi_{2r}$ , to distinguish the left side from the right side. However, the standard  $\Psi_2$  does not contain this information since  $\Psi_2 \in (-\pi/2, \pi/2]$  has a range of  $\pi$  instead of  $2\pi$ . We thus propose the following correlator for each event:

$$v_1\{\Psi_2\} = \langle \cos(\phi - \Psi_2) \rangle. \quad (6)$$

In the above,  $\phi$  is the azimuthal angle of a particle within the narrowed EPD  $\eta$  range,  $\Psi_2$  is the second-order event plane angle, and the bracket  $\langle \rangle$  represents the averaging over particles in the event. We then use the sign of  $v_{1,\text{west}}\{\Psi_2\}$  (for particles within the narrowed EPD range  $3.5 < \eta < 5.09$ ) to determine the directional second-order event plane angle  $\Psi_{2r}$ :

$$\begin{aligned} \Psi_{2r} &= \Psi_2 & \text{if } v_{1,\text{west}}\{\Psi_2\} \geq 0, \\ &= \Psi_2 + \pi & \text{otherwise.} \end{aligned} \quad (7)$$

For the  $v_2$  splitting analysis, we treat the  $\Psi_{2r}$  angle as the  $x$ -axis; e.g., any hadron with  $\cos(\phi - \Psi_{2r}) > 0$  belongs to the  $p_x > 0$  group.

Figure 7(a) shows the event-by-event correlation between  $v_1\{\Psi_2\}$  from particles within  $3.5 < \eta < 5.09$  and that from particles within  $-5.09 < \eta < -3.5$  from the AMPT model (with randomized reaction plane angle) for Au+Au collisions at 11.5A GeV. We see that  $v_{1,\text{west}}\{\Psi_2\}$  is significantly anticorrelated with  $v_{1,\text{east}}\{\Psi_2\}$ . Figure 7(b) shows the event-by-event correlation between the reconstructed  $\Psi_1$  and  $\Psi_{2r}$  angles, which is strong and positive as expected. Therefore, we use  $\Psi_{2r}$  as the event

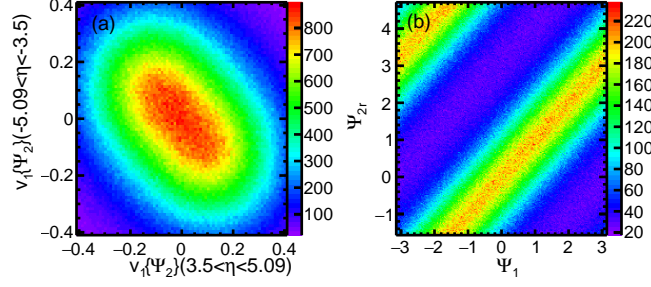


FIG. 7. AMPT results on the event-by-event (a)  $v_1\{\Psi_2\}$  for particles within  $-5.09 < \eta < -3.5$  versus that within  $3.5 < \eta < 5.09$ , and (b) reconstructed  $\Psi_{2r}$  versus  $\Psi_1$  for minimum bias Au+Au collisions at 11.5A GeV.

plane angle for the  $v_2$  splitting analysis in this section, where  $v_1$  and  $v_2$  are calculated using the two-subevent method [30]:

$$v_n^a\{\Psi_{2r}\} = \frac{\langle \langle \cos[n(\phi - \Psi_{2r}^b)] \rangle \rangle}{R_n^{\text{sub}}\{\Psi_{2r}^b\}}. \quad (8)$$

Note that  $c_3$  is calculated similarly, and the two-subevent method removes the self-correlation between  $\Psi_{2r}$  and the flow coefficients ( $v_1$ ,  $v_2$ , and  $c_3$ ) calculated relative to  $\Psi_{2r}$ . The two subevents here are from  $0 < \eta < 2$  and  $-2 < \eta < 0$ , and the subevent resolutions are calculated as  $R_n^{\text{sub}}\{\Psi_{2r}\} = \sqrt{\langle \cos[n(\Psi_{2r}^a - \Psi_{2r}^b)] \rangle}$ .

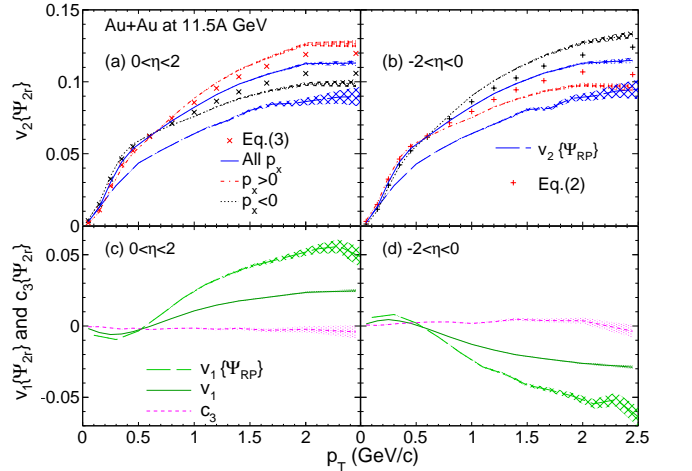


FIG. 8. Same as Fig. 5 for results after applying resolution corrections but relative to the event plane angle  $\Psi_{2r}$ .

We show in Fig. 8(a) and (b) the  $v_2$  splitting results of charged hadrons within  $0 < \eta < 2$  and  $-2 < \eta < 0$ , respectively, after the resolution  $R_2^{\text{sub}}\{\Psi_{2r}\}$  ( $=0.433$  here) is applied. The overall  $v_1\{\Psi_{2r}\}$  and  $c_3\{\Psi_{2r}\}$  results are shown in Figs. 8(c) and (d), after the resolutions  $R_1^{\text{sub}}\{\Psi_{2r}\}$  ( $=0.715$  here) and  $R_3^{\text{sub}}\{\Psi_{2r}\}$  ( $=0.357$  here) are applied to correct  $v_1$  and  $c_3$ , respectively. The cross symbols and plus symbols represent respectively the expectations

of Eq.(3) and Eq.(2) based on the corresponding overall corrected  $v_2$  and  $v_1$ . Similarly to Fig. 5, Eqs.(2)-(3) fail to describe the split  $v_2$  curves, and this is due to the different resolution values. In addition, we see that although  $v_2\{\Psi_{2r}\}$  are still higher than  $v_2\{\Psi_{RP}\}$  (long dashed curves in the upper panels), the difference between them is smaller than that between  $v_2\{\Psi_1\}$  and  $v_2\{\Psi_{RP}\}$ . Furthermore, unlike  $v_1\{\Psi_1\}$ ,  $v_1\{\Psi_{2r}\}$  is much lower than  $v_1\{\Psi_{RP}\}$  (long dashed curves in the lower panels).

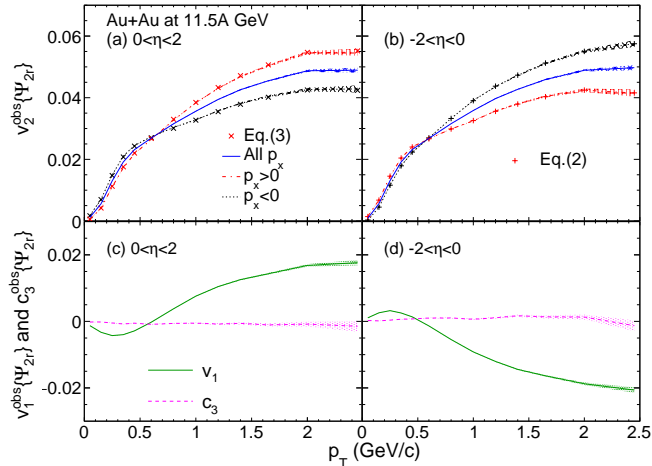


FIG. 9. Same as Fig. 6 for results without the resolution corrections but relative to the event plane angle  $\Psi_{2r}$ .

Figure 9 shows the raw results relative to  $\Psi_{2r}$  without resolution corrections. Similarly to the raw results relative to  $\Psi_1$  shown in Fig. 6, the raw  $v_2$  split curves relative to  $\Psi_{2r}$  also agree well with the expectations from Eqs.(2)-(3). As a result, the raw overall  $v_2$  extracted with Eq. (3) from the split  $v_2$  measurements relative to  $\Psi_{2r}$  can be corrected with its event plane resolution to yield the corrected  $v_2$ , which will be equivalent to the standard  $v_2\{\Psi_2\}$ . Therefore, the  $v_2$  splitting measurement should be feasible experimentally, using either the first-order event plane  $\Psi_1$  or the directional second-order event plane  $\Psi_{2r}$ .

Figure 10 shows in panel (a) the  $v_2(p_x>0)$  and  $v_2(p_x<0)$  results of charged hadrons within  $0 < \eta < 2$  from the AMPT model for minimum bias Au+Au collisions at 11.5A GeV relative to three angles: the first-order event plane angle  $\Psi_1$ , the directional second-order event plane angle  $\Psi_{2r}$ , and the theoretical reaction plane angle  $\Psi_{RP}$ . The corresponding results for the  $v_2$  splitting, i.e.,  $v_2(p_x>0) - v_2(p_x<0)$ , are shown in panel (b). We see in panel (a) that the  $v_2(p_x>0)$  and  $v_2(p_x<0)$  results (after applying the resolution correction) relative to the event plane angle  $\Psi_{2r}$  agree better with, although are somewhat higher than, the results relative to the reaction plane. From Fig. 10 (b), it is clear that the  $v_2$  splitting relative to the event plane angle  $\Psi_{2r}$  is much closer to that relative to the reaction plane. Therefore, the directional second-order event plane  $\Psi_{2r}$  is preferred from the

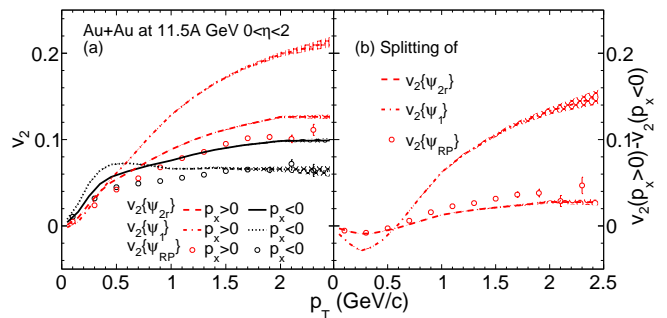


FIG. 10. (a) The split  $v_2$  and (b) the  $v_2$  splitting  $v_2(p_x>0) - v_2(p_x<0)$  of charged hadrons within  $0 < \eta < 2$  relative to the event plane angle  $\Psi_1$ ,  $\Psi_{2r}$ , and the theoretical reaction plane angle  $\Psi_{RP}$  (circles) as functions of the transverse momentum from the AMPT model for minimum bias Au+Au collisions at 11.5A GeV.

perspective of measuring the  $v_2$  splitting.

## V. DISCUSSIONS

We emphasize that the string melting AMPT model currently cannot describe the directed flow well [32, 33], even though the model typically well describes the elliptic and triangular flows. Therefore, results of the  $v_2$  splitting from the AMPT model in this study are used primarily to demonstrate the relationship between the  $v_2$  splitting and  $v_1$  as shown in Eqs.(2)-(3). The AMPT results of  $v_1(p_T)$  and the  $v_2$  splitting here are not intended as quantitative predictions for the experimental observables; instead, they represent the exploration of the  $v_2$  splitting possibilities. The inability of the string melting AMPT model to reproduce  $v_1$  observables is related to its neglect of the finite (i.e., nonzero) nuclear thickness along the beam ( $z$ ) direction, because the nuclear  $z$ -width varies along the  $x$ -direction and would thus affect the tilted shape of the created matter. In addition, the finite nuclear thickness has been shown to significantly affect the energy density of the dense matter at low energies [34, 35] and the dynamics at finite rapidities even at high energies [36].

It has been realized in recent years that non-central heavy ion collisions are affected by other interesting effects such as a strong electromagnetic field [37, 38] and vorticity field [39]. For example, a significant fraction of the initial total angular momentum in a non-central heavy ion collision is deposited into the created dense matter and thus creates a global vorticity field, which leads to global polarization of hyperons and spin alignment of vector mesons that have been observed [39–41]. Since we find that the left-right  $v_2$  splitting is mostly due to  $v_1$ , it will be interesting to study how the vorticity field affects the development of  $v_1$  and consequently the  $v_2$  splitting [17]. Note that the global vorticity field and  $v_1$  share several similarities; e.g., the magnitude is

usually larger at larger rapidities, and they both have a left-right antisymmetry.

More generally, it will be useful to study the correlations and relationships among anisotropic flows, the electromagnetic field, and the vorticity field. For example, the splitting of charm and anti-charm directed flows has been proposed as a result of the electromagnetic field [42]. The rotation of the created matter has also been shown to affect the flow pattern, especially the directed flow [43]. The dynamics that generates  $v_1$  is quite complicated, as  $v_1$  depends on the equation of state, mean-field potentials, particle rescatterings, shadowing from spectator nucleons, and the tilt of the created matter in the  $x-z$  plane [44–46]. On the other hand,  $v_2$  depends on the geometry of the created matter in the  $x-y$  plane. Therefore, the left-right  $v_2$  splitting reflects the three-dimensional geometry and dynamical evolution of the dense matter.

## VI. SUMMARY

We have examined the left-right splitting of the elliptic flow, on opposite sides of the impact parameter axis, that has been recently proposed as a new effect due to the global vorticity in non-central heavy ion collisions. In this study, we find that this  $v_2$  splitting is due to the non-zero directed flow  $v_1$  at finite rapidities and approximately given by  $8v_1(1 - 3v_2)/(3\pi)$ . Therefore, the splitting is expected to depend sensitively on the transverse momentum, rapidity range, and particle species.

We also use the string melting version of a multi-phase transport model, which automatically includes the vorticity field and flow fluctuations and usually describes well the elliptic and triangular flows. Our model results con-

firm the existence of the  $v_2$  splitting at finite rapidities on both parton and hadron levels above certain transverse momenta. We also find that the relative splitting may be significant even for central heavy ion collisions, the splitting within a fixed (pseudo)rapidity range is expected to decrease with the colliding energy, and the splitting at large rapidity may be significant even at LHC energies. In addition, we find that the  $v_2$  splitting should be measurable experimentally with the event plane method using either the first- or second-order event plane, and that the analytical expectations for the  $v_2$  splitting apply to the raw  $v_2$  and  $v_1$  (i.e., before applying their respective event plane resolutions) in each case. Therefore, one can extract the raw overall  $v_1$  and  $v_2$  from the  $v_2$  splitting measurements. In the typical case where  $c_3 \simeq 0$ , after applying event plane resolutions the corrected overall  $v_1$  is equivalent to the usual  $v_1$  if the  $v_2$  splitting is measured relative to the first-order event plane, while the corrected overall  $v_2$  is equivalent to the usual  $v_2$  if the  $v_2$  splitting is measured relative to the second-order event plane. From the perspective of measuring the split  $v_2$ , the directional second-order event plane  $\Psi_{2r}$  is preferred since its  $v_2$  results agree better with those relative to the reaction plane. The left-right  $v_2$  splitting, as a complementary observable to the standard flow observables, will benefit the studies of the three-dimensional geometry and dynamical evolution of the dense matter created in heavy ion collisions.

## ACKNOWLEDGEMENT

C.Z. acknowledges support from the Chinese Scholarship Council. This work is supported the National Science Foundation under Grant No. 2012947 (Z.-W.L.).

- 
- [1] E. V. Shuryak, *Phys. Lett. B* **78**, 150 (1978).
  - [2] S. Voloshin and Y. Zhang, *Z. Phys. C* **70**, 665 (1996).
  - [3] B. Alver and G. Roland, *Phys. Rev. C* **81**, 054905 (2010), [erratum: *Phys. Rev. C* **82**, 039903 (2010)].
  - [4] K. H. Ackermann *et al.* (STAR), *Phys. Rev. Lett.* **86**, 402 (2001).
  - [5] S. S. Adler *et al.* (PHENIX), *Phys. Rev. Lett.* **91**, 182301 (2003).
  - [6] K. Aamodt *et al.* (ALICE), *Phys. Rev. Lett.* **105**, 252302 (2010).
  - [7] C. Aidala *et al.* (PHENIX), *Nature Phys.* **15**, 214 (2019).
  - [8] S. Chatrchyan *et al.* (CMS), *Phys. Lett. B* **724**, 213 (2013).
  - [9] K. Dusling, M. Mace, and R. Venugopalan, *Phys. Rev. Lett.* **120**, 042002 (2018).
  - [10] M. Mace, V. V. Skokov, P. Tribedy, and R. Venugopalan, *Phys. Rev. Lett.* **121**, 052301 (2018), [erratum: *Phys. Rev. Lett.* **123**, 039901 (2019)].
  - [11] L. He, T. Edmonds, Z.-W. Lin, F. Liu, D. Molnar, and F. Wang, *Phys. Lett. B* **753**, 506 (2016).
  - [12] Z.-W. Lin, L. He, T. Edmonds, F. Liu, D. Molnar, and F. Wang, *Nucl. Phys. A* **956**, 316 (2016).
  - [13] A. Kurkela, U. A. Wiedemann, and B. Wu, *Phys. Lett. B* **783**, 274 (2018).
  - [14] A. Kurkela, U. A. Wiedemann, and B. Wu, *Eur. Phys. J. C* **79**, 965 (2019).
  - [15] R. D. Weller and P. Romatschke, *Phys. Lett. B* **774**, 351 (2017).
  - [16] U. W. Heinz and J. S. Moreland, *J. Phys. Conf. Ser.* **1271**, 012018 (2019).
  - [17] Z. Chen, Z. Wang, C. Greiner, and Z. Xu, (2021), arXiv:2108.12735 [hep-ph].
  - [18] Z.-W. Lin, C. M. Ko, B.-A. Li, B. Zhang, and S. Pal, *Phys. Rev. C* **72**, 064901 (2005).
  - [19] C. Zhang, L. Zheng, S. Shi, and Z.-W. Lin, *Phys. Rev. C* **104**, 014908 (2021).
  - [20] Z.-W. Lin and C. M. Ko, *Phys. Rev. C* **65**, 034904 (2002).
  - [21] G.-L. Ma and Z.-W. Lin, *Phys. Rev. C* **93**, 054911 (2016).
  - [22] Y. Jiang, Z.-W. Lin, and J. Liao, *Phys. Rev. C* **94**, 044910 (2016), [erratum: *Phys. Rev. C* **95**, 049904 (2017)].

- [23] H. Li, L.-G. Pang, Q. Wang, and X.-L. Xia, Phys. Rev. C **96**, 054908 (2017).
- [24] Y. He and Z.-W. Lin, Phys. Rev. C **96**, 014910 (2017).
- [25] C. Zhang, L. Zheng, F. Liu, S. Shi, and Z.-W. Lin, Phys. Rev. C **99**, 064906 (2019).
- [26] L. Zheng, C. Zhang, S. S. Shi, and Z.-W. Lin, Phys. Rev. C **101**, 034905 (2020).
- [27] J. Xu, L.-W. Chen, C. M. Ko, and Z.-W. Lin, Phys. Rev. C **85**, 041901 (R) (2012).
- [28] J. Xu, T. Song, C. M. Ko, and F. Li, Phys. Rev. Lett. **112**, 012301 (2014).
- [29] A. M. Poskanzer and S. A. Voloshin, Phys. Rev. C **58**, 1671 (1998).
- [30] S. A. Voloshin, A. M. Poskanzer, and R. Snellings, Landolt-Bornstein **23**, 293 (2010).
- [31] J. Adams *et al.*, Nucl. Instrum. Meth. A **968**, 163970 (2020).
- [32] K. Nayak, S. Shi, N. Xu, and Z.-W. Lin, Phys. Rev. C **100**, 054903 (2019).
- [33] K. Nayak (STAR), Nucl. Phys. A **1005**, 121855 (2021).
- [34] Z.-W. Lin, Phys. Rev. C **98**, 034908 (2018).
- [35] T. Mendenhall and Z.-W. Lin, Phys. Rev. C **103**, 024907 (2021).
- [36] C. Shen and B. Schenke, Phys. Rev. C **97**, 024907 (2018).
- [37] V. Voronyuk, V. D. Toneev, W. Cassing, E. L. Bratkovskaya, V. P. Konchakovski, and S. A. Voloshin, Phys. Rev. C **83**, 054911 (2011).
- [38] W.-T. Deng and X.-G. Huang, Phys. Rev. C **85**, 044907 (2012).
- [39] L. Adamczyk *et al.* (STAR), Nature **548**, 62 (2017).
- [40] Z.-T. Liang and X.-N. Wang, Phys. Rev. Lett. **94**, 102301 (2005), [erratum: Phys. Rev. Lett. **96**, 039901 (2006)].
- [41] S. Acharya *et al.* (ALICE), Phys. Rev. Lett. **125**, 012301 (2020).
- [42] S. K. Das, S. Plumari, S. Chatterjee, J. Alam, F. Scardina, and V. Greco, Phys. Lett. B **768**, 260 (2017).
- [43] L. P. Csernai, D. D. Strottman, and C. Anderlik, Phys. Rev. C **85**, 054901 (2012).
- [44] R. J. M. Snellings, H. Sorge, S. A. Voloshin, F. Q. Wang, and N. Xu, Phys. Rev. Lett. **84**, 2803 (2000).
- [45] C. Zhang, J. Chen, X. Luo, F. Liu, and Y. Nara, Phys. Rev. C **97**, 064913 (2018).
- [46] Y. Nara, H. Niemi, A. Ohnishi, and H. Stöcker, Phys. Rev. C **94**, 034906 (2016).